Original article

Study of the pore size influence on infiltration of porous media considering capillary effect

Zhao Lu[1,2], Changnv Zeng[2]*, Yiyang Zhang[2], Hu Lu[3]*

[1]*HKUST Shenzhen-Hong Kong Collaborative Innovation Research Institute, Shenzhen 518000, P. R. China*

[2]*Department of Civil Engineering, He'nan University of Technology, Zhengzhou 450052, P. R. China*

[3]*School of Construction Engineering, Shenzhen Polytechnic University, Shenzhen 518107, P. R. China*

Abstract:
The significance of pore size as a determinant in two-phase flow dynamics is widely acknowledged. However, the micro-scale behavior of flow including pore channel capillary and air-water interface development are not systematically interpreted due to the limitation of test and computation methodologies. In the present study, an investigation was conducted into the impact of varying pore throat widths on the flow of a two-phase fluid. For the investigation, numerical simulations were integrated with microfluidic experimentation to provide a comprehensive analysis. The results indicate that large pore diameters in porous media are associated with accelerated infiltration rates, leading to quicker stabilization. However, an inverse correlation exists between pore throat diameter and seepage area, with larger diameters yielding larger residual air areas. In this investigation, the "queuing effect" was observed across all tests, irrespective of pore throat diameter. Water initially permeated the central region of the pore network, sequentially inducing a breakthrough in adjacent pores. It was found that smaller pore throat diameters necessitated higher breakthrough pressures. Consistently, under unchanged inlet flow rates, narrower channels exhibited greater capillary resistance, impeding water flow. Specifically, for the four models with increasing pore throat widths, the critical capillary resistances are decreasing continuously from 87.6 to 38.2 Pa ultimately.

1. Introduction

Two-phase flow in porous media is prevalent in various significant scientific phenomena within both industrial production and natural environments. Examples include soil infiltration, carbon sequestration, and oil recovery processes (Culligan et al., 2000; Morrow et al., 2001; Bachu, 2015). The physical process of two-phase flow involves the invasion of fluid into porous media to displace another immiscible fluid. A major difficulty in achieving a good understanding of two-phase flow in the porous media is the large number of parameters potentially involved. These encompass the surface tension of the fluid, the wetting characteristics of the porous medium, the viscosity of the fluid, the size of the pore structure, as well

as the porosity and permeability of the porous media. Cai et al. (2014) have conducted the study in two phase flow, and provided a fundamental interpretation of capillary effect for the following study.

Recently, there has been considerable focus on investigating the characteristics of two-phase flow in porous media at the pore scale (Golparvar et al., 2018; Cai et al., 2022; Zhang et al., 2024). Such attention has led to numerous experimental and numerical simulation studies. However, previous research has faced challenges in directly observing the two-phase flow process and phase distribution within porous media due to technical limitations. As such, numerical simulation has emerged as a primary research methodology in this domain. Various techniques such as pore network modeling, the lattice

Boltzmann method, volume of fluid method, level set method, phase field method (e.g., Hirt and Nichols, 1981; Takada and Tomiyama, 2006; Wang et al., 2015; Li et al., 2016; Cai et al., 2021), among others, are commonly employed to investigate two-phase flow characteristics in porous media. Compared to other numerical methods, the PFM requires less computing resources to obtain higher computational accuracy (Mirjalili et al., 2017). And phase field method can accurately capture more physical details. Especially in complex porous media, the phase field method can provide more realistic pressure gradients and fluid profiles (Amiri and Hamouda, 2023). Using the phase field method, Hizir and Hardt (2014) found that droplet adhesion to surfaces was stronger when the contact angle was low. Zhu et al. (2016) determined the position of the interface between water and oil slugs by means of the phase field method. They also proposed critical capillary numbers as functions of the static contact angle and viscosity ratio of the two phases. Rokhforouz et al. (2017) investigated micro-scale mechanisms during counter-current imbibition processes by using the phase field method, as well as the influence of multiple factors such as interfacial tension.

The field of microfluidics has witnessed significant development alongside technological advancements. Widely utilized for investigating micro-scale phenomena across physical, chemical, biological, medical, and environmental domains, microfluidics offers numerous advantages (Gravesen et al., 1993; Stone and Kim, 2001; Beebe et al., 2002). These include reduced reagent consumption, accelerated sample processing, enhanced sensitivity, greater portability, improved visualization, increased integration, and automation capabilities (Bhagat et al., 2010). Using soft lithography techniques, researchers can etch designed porous networks onto microfluidic chips to mimic pore media structures. These microfluidic chips serve as effective platforms for investigating two-phase flow behaviors within porous media in research studies (Wei et al., 2024). Through combining microfluidic experiments and pore-scale simulations, Hu et al. (2019) explored the impact of disorder on the quasi-static displacement from weak imbibition to strong drainage, and derived a theoretical model to describe the cross-over zone between compact displacement and capillary fingering in porous media. Cottin et al. (2010) scrutinized the impact of capillary numbers on the mechanism of non-wetting fluid infiltration and subsequent drainage. They accomplished this by constructing straight microchannels with varying pore sizes. Through their experiments, they formulated a rudimentary model capable of elucidating the observed capillary fingering.

The pore size is the main factor affecting the infiltration of porous media. In general, water permeates more slowly in dense soils. On the other hand, water permeates more faster through loose soils. Cao et al. (2016) indicated through model experiments that the impact of pore size distribution on the displacement of supercritical CO_2 and brine is relevant. Zhan et al. (2021) and Li et al. (2022, 2023) explored the physical behavior of the capillary barrier effect in microfluidic chips by etching fine-coarse porous media structures with different pore topologies (square and honeycomb) as well as sizes. In previous studies, the variation of flow pattern from finger-flow type to compact invasion type were discussed, as the water saturation and trapped air patches were the main analyzing parameters. However, the microscopic details of flow process were missing including the air-water pressure development and flow velocity change between the particles in the infiltration domain. The capillary effect of flow through the pore channel was not systematically present and analyzed due to the missing of key parameters. On the other hand, the pore size variability has been considered as one critical parameter in determining the flow process, while the comparative study including experiment and numerical simulation was seldomly reported. Therefore, the quantitative research on pore size of circular structures is required, and the mechanism of fluid infiltration in different pore sizes needs to be further discussed. In addition, during the flow process, the front edge of the two-phase interface will undergo capillary effects. The capillary pressure will affect the formation of pores to a certain extent (Wang et al., 2017; Patiño and Nieto-Londoño, 2021). Similarly, the width of the pore structure also affects the size of the capillary pressure, further influencing the evolution of the phase morphology during the fluid's percolation through the porous medium. The variation of water pressure during infiltration is essential to study the permeability of porous media. Vincent-Dospital et al. (2022) conducted an analysis of two-phase flow in porous media with a grain size gradient, and the research findings indicated that the evolution of water morphology is associated with the pressure gradient necessary for the fluid to enter the pores and the distribution of pore diameter sizes.

The aim of the present study was to explore the micro-scale behavior of water flow in different pore sizes. Based on the phase field method and keeping the porosity consistent, the water flow process in four porous media with different pore sizes was simulated. To validate the accuracy of the simulations, a microfluidic chip of identical dimensions to the simulated model was etched before experiments were conducted. The experimental and simulation results exhibited good agreement. Subsequently, an analysis was conducted to elucidate the impact of differing pore sizes on the infiltration behavior, examining water morphology, pore pressure, and fluid velocity as key factors.

2. Materials and methods

The simulated governing equations, model geometry, model meshing and model verification are presented. All the simulation models in the present study were conducted using the phase field method in the COMSOL Multiphysics software.

2.1 Numerical simulation

2.1.1 Phase-field method

The phase field method involves solving the Navier-Stokes equation of momentum conservation and the continuity equation of mass conservation, and describing the process of two-phase separation by coupling the Cahn-Hilliard equation to capture the changes in the interface position. The Cahn-Hilliard is expressed as follows (Badalassi et al., 2023):

$$\frac{\partial \phi}{\partial t} + u \cdot \nabla \phi = \nabla \cdot \frac{\gamma \lambda}{\varepsilon^2} \nabla \psi \tag{1}$$

$$\psi = -\nabla \cdot \mathscr{E}^2 \nabla \phi + (\phi^2 - 1) \phi + \left(\frac{\varepsilon^2}{\lambda}\right) \frac{\partial f_{ext}}{\partial \phi} \tag{2}$$

where u is the fluid flow velocity, γ represents mobility, λ represents the mixed energy density, ε is a capillary width that scales with the interfacial thickness, f_{ext} represents the external free energy. In the described equations, two additional equations are solved to track the interface. These arise from the use of the phase field method and comprise the phase-field variable (ϕ) and phase-field help variable (ε). The range of ϕ varies from -1 to 1.

Navier-Stokes describes the flow process of a two-phase fluid by introducing surface tension as a volume force into Navier-Stokes. The equations are:

$$\rho \frac{\partial u}{\partial t} + \rho(u \cdot \nabla)u = \nabla \left[-pI + \mu \left(\nabla u + (\nabla u)^T\right)\right] + F_g + F_{st} \tag{3}$$

$$\rho \nabla \cdot u = 0 \tag{4}$$

where ρ is the fluid density, ∇ is the dynamic viscosity, p is the pressure and T is the temperature, and F_{st} represent gravity and surface tension respectively.

Navier-Stokes and Cahn-Hilliard are solved simultaneously with the continuity equation, which is:

$$\frac{\partial p}{\partial t} + \nabla \cdot (\rho u) = 0 \tag{5}$$

In the described equations, Fluid velocity (u), dynamic viscosity (∇), density (ρ), gravity force (F_g) and surface tension (F_{st}) are defined according to the external free energy (f_{ext}), density ($\rho_{1,2}$) and dynamic viscosity ($\nabla_{1,2}$) of the two fluids.

$$\rho = \rho_1 (1 - V_{f2}) + \rho_2 (V_{f2}) \tag{6}$$

$$\mu = \mu (1 - V_{f2}) + \mu (V_{f2}) \tag{7}$$

$$F_g = \rho g \tag{8}$$

$$F_{st} = \left(G - \frac{\partial f_{ext}}{\partial \phi}\right) \nabla \phi \tag{9}$$

where G is the chemical potential defined in terms of mixing energy density (λ) and capillary width (ε) as:

$$G = \lambda \left(-\nabla^2 \phi + \frac{\phi(\phi - 1)}{\varepsilon^2}\right) + \frac{\partial f_{ext}}{\partial \phi} \tag{10}$$

and V_{f2} is the volume fraction of fluid 2, defined as:

$$V_{f2} = \frac{1 + \phi}{2} \tag{11}$$

The relationship between the mixed energy density (λ), the capillary width (ε) and the surface tension coefficient (σ) is:

$$\sigma = \frac{2\sqrt{2}}{3} \frac{\lambda}{\varepsilon} \tag{12}$$

The relationship between the mobility (γ), the capillary width (ε) and the mobility tuning parameter (χ) is:

Table 1. Types of numerical simulation models and internal structural parameters.

No.	d (mm)	D (mm)	L_C (mm)	ε	V
d1	0.36	1.08	0.53	0.553	3.3×10^{-3}
d2	0.8	2.16	1.08	0.553	3.3×10^{-3}
d3	1	2.9	1.41	0.553	3.3×10^{-3}
d4	1.44	4.32	2.12	0.553	3.3×10^{-3}

$$\chi = \frac{\gamma}{\varepsilon^2} \tag{13}$$

2.1.2 Model geometry

As shown in Fig. 1, the geometry of the simulated domain is illustrated. Four two-dimension rectangular porous media, each measuring 23.04 × 11.52 mm, were constructed to simulate matrix blocks. The grains were depicted by an isosceles triangular array of circles with identical diameters. The matrix porosity of the four models was $\varepsilon = 0.553$. The particle pore throat width of model d1 ($d = 0.36$ mm) was used as the standard value, and the pore throat widths of the other three models were d2 ($d = 0.8$ mm), d3 ($d = 1.0$ mm), and d4 ($d = 1.4$ mm), respectively. Above specific parameters of the minimum spacing d of adjacent grains and the spacing L_C of diagonal grains are shown in Table 1. D indicates the particle diameter which is consistent with the change of pore throat widths. The upper boundary of the model was set as the entrance, the lower boundary was set as the exit, and the left and right walls were set with no slip boundary conditions. Additionally, the inlet velocity of all simulations was 3.3e × 10^{-4} m/s.

2.1.3 Model meshing

The accuracy of the solution outcomes is significantly influenced by the level of mesh refinement. Finer meshes yield solutions closer to reality. In the present study, an unstructured free triangle mesh with a size of 0.2 mm was employed for mesh division. The meshes were calibrated using fluid dynamics. The numbers of meshes used in the d1-d4 models were 23,484, 16,066, 13,489 and 16,307, respectively. The partial mesh division diagram is presented in Fig. 2.

2.2 Model verification

The two-phase flow with four pore sizes were analyzed through the comparative study of numerical simulation and microfluidic test, as the model boundary condition were referred from the test condition. Specifically, one constant flow velocity was applied at the inlet boundary, and the outlet boundary was settled as open boundary. A microfluidic chip was designed to verify the accuracy of the simulation results. In the experiment, water was injected into the microfluidic chip at 100ul/min (Darcy's velocity in the chip was calculated to be 3.3×10^{-4} m/s) by an injection pump, and the movement of water-air interface was recorded in real time by an information acquisition device.

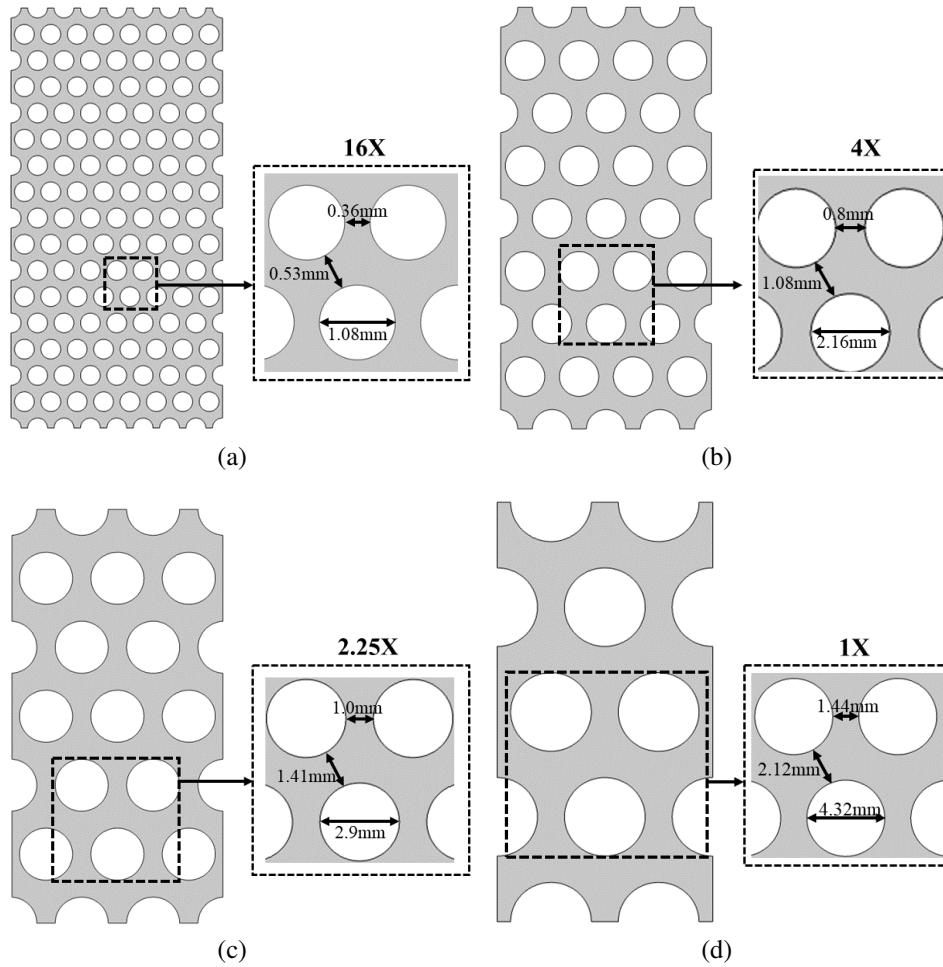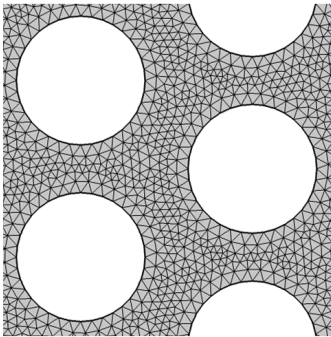**Fig. 1**. Schematic diagram of physical model. (a) d1 model, (b) d2 model, (c) d3 model, (d) d4 model.

Fig. 2. Partial mesh division diagram.

2.2.1 Experimental set-up

The experimental set-up used in the present study was composed of three components: A microfluidic injection system, a microscopic model observation system and a microfluidic chip.

1) The microfluidic injection system consisted of an injection pump (PHD2000, Harvard Apparatus, US) and a polypropylene syringe. The injection pump could provide an injection rate of 00033 μl/min to 205.30 ml/h.

The microfluidic injection pump injected water into the microfluidic chip at a constant flow rate.

2) The microscopic model observation system consisted of a stereoscopic microscope (T2-3M180, Aosvi, z) and an information acquisition device. A camera with image and video capture functions was installed in the microscope, and the stored data could be uploaded to the information acquisition device for display.

3) The physical diagram of the microfluidic chip is shown in Fig. 3(a). The microfluidic chip internal structure contained an inlet, upstream buffer channel, internal porous network, downstream buffer channel and an outlet, as presented in Fig. 3(b). The microfluidic chip was fabricated from transparent material with high transmittance, namely polydimethylsiloxane. Inside, various pore structures were etched to emulate soil pore structures. In the present study, the size of the pore structure was consistent with the numerical model d1. When water was injected into the chip by the injection pump, it first filled the buffer channel and distributed the flow evenly. The whole test process was conducted at room temperature (about 20°C).
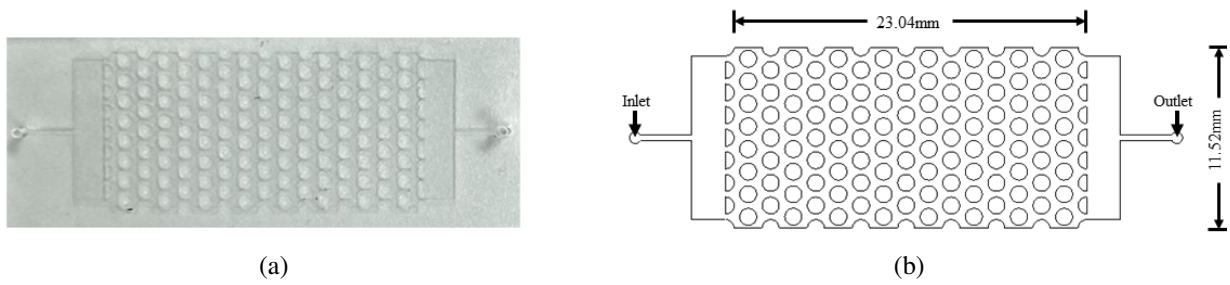
(a)   (b)

Fig. 3. Microfluidic test device diagram. (a) Fabricated pore structure in the microfluidic chip and (b) designed pore structure in the microfluidic chip.

2.2.2 Experimental procedures

The experiments involved injecting deionized water at a fixed rate into a dry microfluidic chip until the water-air interface reached the outlet. The entire process of water transport during injection was recorded using a microscope and uploaded to the information acquisition device. Prior to the experiment, the microfluidic chip was cleaned by injecting deionized water with an injection rate of 500 μl/min for 2 min, and then over-dried at 85 °C for 2 h. The microfluidic chip was held at laboratory temperature for 2 h to reach thermal equilibrium after drying. Subsequently, the experimental system was assembled accordingly and the experiment was started. The microfluidic chip was filled with air before the experiment. Then, the tests commenced by injecting deionized water into the chip at a constant injection rate $3.3e^{-4}$ m/s.

2.2.3 Experimental and simulation results

As illustrated in Fig. 4, the comparison of water intrusion patterns obtained from model d1 (pore throat width 0.36 mm) experiments and simulations is plotted at several typical moments, as L_w is the distance from the water front to the inlet boundary, and L_0 is the total length of the pore structure in the flow direction (Hu et al., 2017). As shown in Fig. 4, some residual air distribution was present in the test process, but the overall infiltration trend was basically consistent with the simulation results. Therefore, the belief of the present authors is that the adopted PFM was sufficient to demonstrate the accuracy of the simulation.

3. Numerical results

3.1 Effect of pore size on water infiltration process

3.1.1 Evolution of the water morphology

Two-phase distribution at representative moments for the four model are exhibited in Fig. 5. An observation can be made that different pore sizes induced a significant effect in the water morphology. In general, water infiltration in models with finer pore sizes tends to present a more uniform water-air interface. As shown in Fig. 5, the water advanced progressively in d1 with a relatively flat water-air front. After the water-air interface front reached the narrowest pore in each row, the water did not immediately infiltrate downwards, but instead

moved laterally in the interlayers. This is indicated in the water-air interface diagrams at 5, 15, and 25 s, respectively (Fig. 5, red arrow on d1). At t = 35 s, the water began to prepare forpercolating into the next interlayer after saturating the prior interlayer, indicated by the water-air interface forming a straight line. As the grain size increased, the number of grain rows decreased and the pore size continuously increased, resulting in an uneven advancement process of the water-air interface. As shown in model d4, the overall distribution of the two-phase interface was similar to a circular arc at 15 s (shown by the red dotted line in Fig. 5. Similarly, this characteristic was observed for the water-air interfaces at 25 and 35 s. The described results indicate that fine pores impeded water infiltration more significantly compared to coarse pores. Capillary resistance primarily drives this phenomenon, with resistance magnitude inversely proportional to pore size. Consequently, the water-air interface encountered substantial capillary resistance at the narrowest inter-grain positions, obstructing downward infiltration. Instead, lateral movement occurred, resulting in the formation of a relatively uniform two-phase interface. However, as the pore size increased, the capillary effect became less obvious, thus leading to the phenomenon of uneven water-air interface in model d4.

The uneven advance of the water-air interface in the coarse pore model tended to cause the air to become trapped behind the water front, as shown in the bubble distributions of model d3 at 15 s and model d4 at 35 s (red circle). This is because of the capillary resistance of water passing through the coarse pores during the infiltration process was minimal, facilitating faster flow velocities. This created a significant velocity differential with the infiltration velocity of water at the boundary. Hence, air became trapped behind the water-air interface. Further, the water-air interface of model d4 reached the exit and gradually became stable, while the interface of d1 was still some distance away from the exit at this moment, as shown in Fig. 5. Thus, different pore sizes also exert a certain influence on both the infiltrate length of the water-air interface and the time required for infiltration to stabilize.

3.1.2 Evaluation of the infiltrate effect

To evaluate the effect of pore size on the infiltrate length, the evolutions of the infiltrate length L with elapsed time t for four models were plotted, as shown in Fig. 6. As aforementioned, as the pore size increased, the capillary resistance
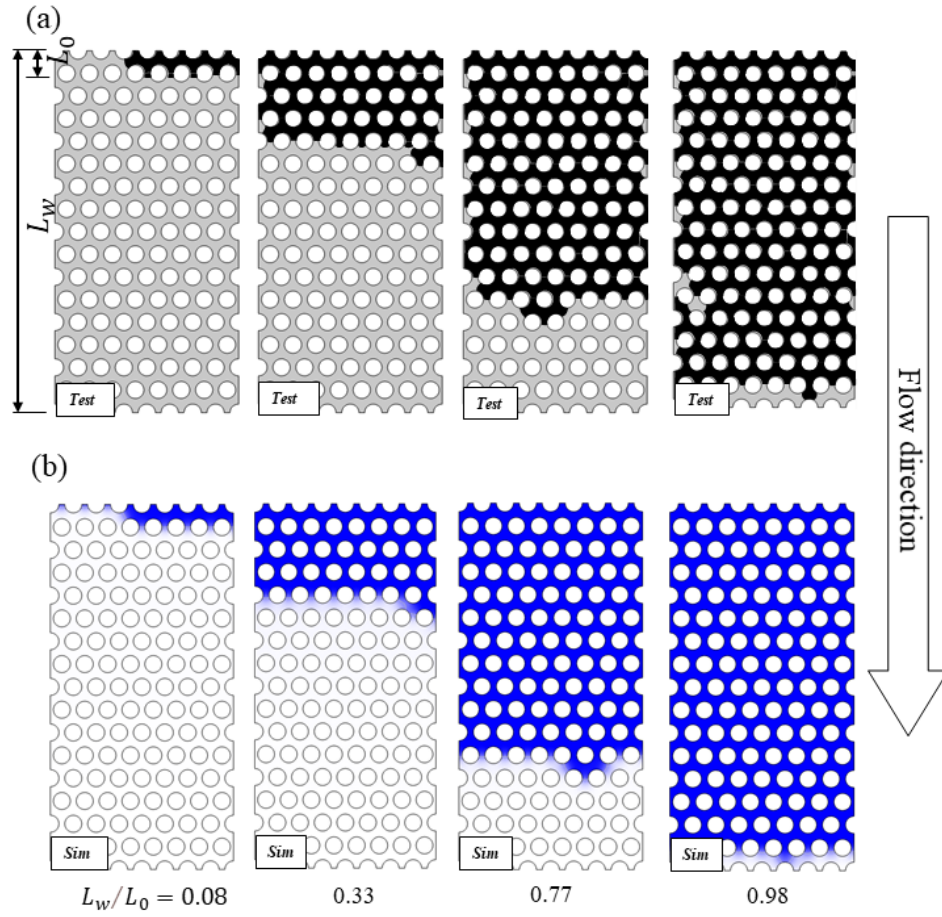
Fig. 4. Comparison of results of microfluidic test and numerical simulation. (a) Microfluidic experiment and (b) numerical simulation.
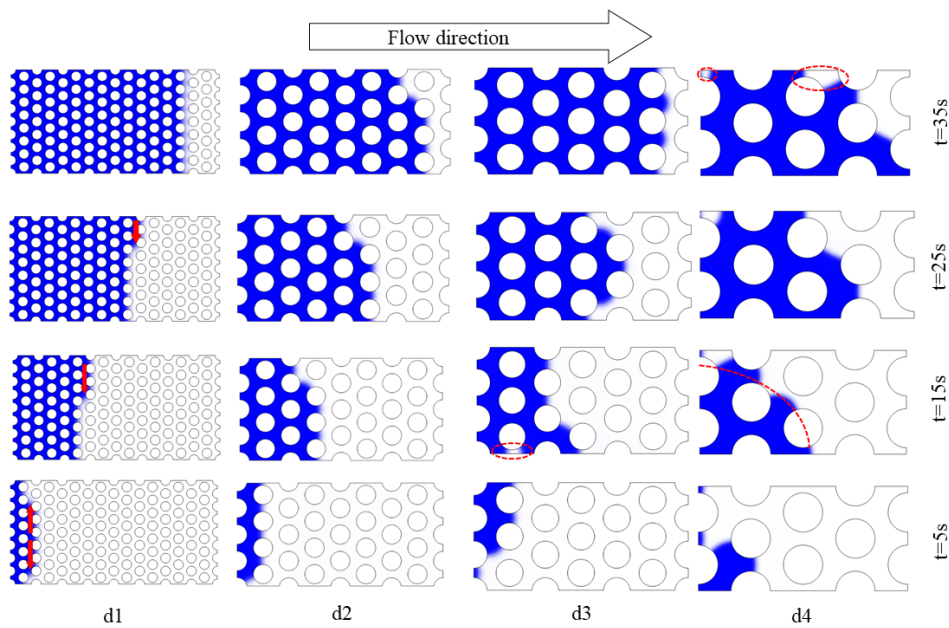

Fig. 5. Diagrams of two-phase distribution at representative moments.

encountered by water during infiltration decreased while flow velocity remained largely unaffected. As such, in model d4, the distance between the water-air front and the inlet was the longest at the same moment. Additionally, the average velocity of water during the infiltration process gradually decreased. In d1, the infiltrate lengths of water-air front corresponding to 5, 15, 25 and 35 s were 2.93, 8.72, 14.48 and 19.19 mm, respectively. Compared with the 5 s, the infiltrate length of water increased by more than 66% at t = 15 s. For the other moments, the increase in water front length between two adjacent moments was 40% and 24% , respectively.

Based on the increase in infiltrate length, it's evident that the average infiltrate velocity of water gradually decreased over the same period of time. This occurred because the inlet water rate remained fixed, leading to a continuous increase in the volume of the water phase within the porous medium. According to the Navier-Stokes equation, the force exerted by fluid flow on a fluid element remained constant, but the flow resistance increased. Consequently, this resulted in a gradual decrease in the average seepage velocity.

From Fig. 7, it is witnessed the final water saturation in the four models and the total infiltration time required to reach stability. The general trend of both curves gradually decreased, indicating that water saturation and the time required for infiltration to reach stability decreased with increasing pore size. Owing to the larger capillary resistance that the water needed to overcome when passing through the fine pores, the flow rate would decrease. Thus, the time required to reach the stable moment was longer with the same porosity, there was a difference of nearly 20% between d1 and d4. In addition, the final water saturation also decreased with the increase in pore size. The difference between the final water saturation in d1 and d4 was about 14% . Such findings can be attributed to the uneven propulsion process of the water-air interface described in Section 3.1.1. The uneven propulsion of the water-air interface easily generated a significant amount of residual air, leading to reduced water saturation and ultimately impacting the infiltration effectiveness.

In summary, under the same porosity, the pore size between grains significantly influenced the water infiltration process. Porous media with a fine pore structure tended to exhibit a flatter water-air interface, with minimal residual air during infiltration. Conversely, porous media characterized by a coarse pore structure exhibited an unstable water-air interface, resulting in trapped air behind the advancing water front and reducing water saturation. Moreover, finer pores required greater capillary resistance for water to pass through, resulting in decreased flow velocity and infiltrate length of the water-air front, consequently prolonging infiltrate time. Further, during the infiltration process, as the volume of the water phase increased, the average infiltrate velocity of water over the same period of time gradually decreased.

3.2 Pressure and seepage field

3.2.1 Pressure field

To comprehensively examine the influence of pore size on the infiltration process, pressure contour distribution maps of
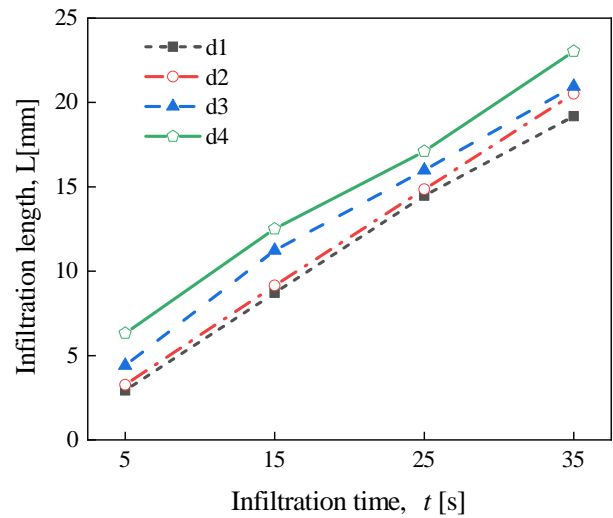

Fig. 6. Evolutions of the infiltrate length L of the water-air front during the water flow process.
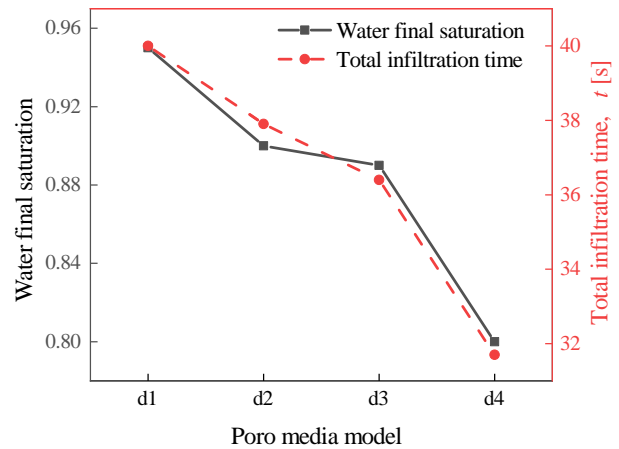

Fig. 7. Final water saturation degree and the time to the stable moment.

d1 and d4 at different moments were plotted, as shown in Fig. 8, respectively. It is evident that the pressure on d1 gradually decreased from the water side to the air side at each moment, with a symmetrically distributed pressure contour along the water-air interface. This observation suggests that there was an equal and balanced pressure difference across both sides of the water-air interface. However, on the air side, certain inflection points (marked by black boxes in Fig. 8 for d1) exhibited denser pressure contour lines, indicating rapid changes in air pressure at these locations and the gradual breakdown of equilibrium. Meanwhile, the water-air interface moved towards regions with higher pressure differences, resulting in increased air resistance to water flow. This intensified the pressure difference on both sides of the interface. Consequently, when the water-air interface broke through any pore, it halted at the narrowest pore in the next row and achieved equilibrium. With insufficient pressure difference for downward flow, water flowed to the upper and lower boundaries, driving the preceding row of water-air interface, which was in equilibrium, to break through pores sequentially. This cycle continued until
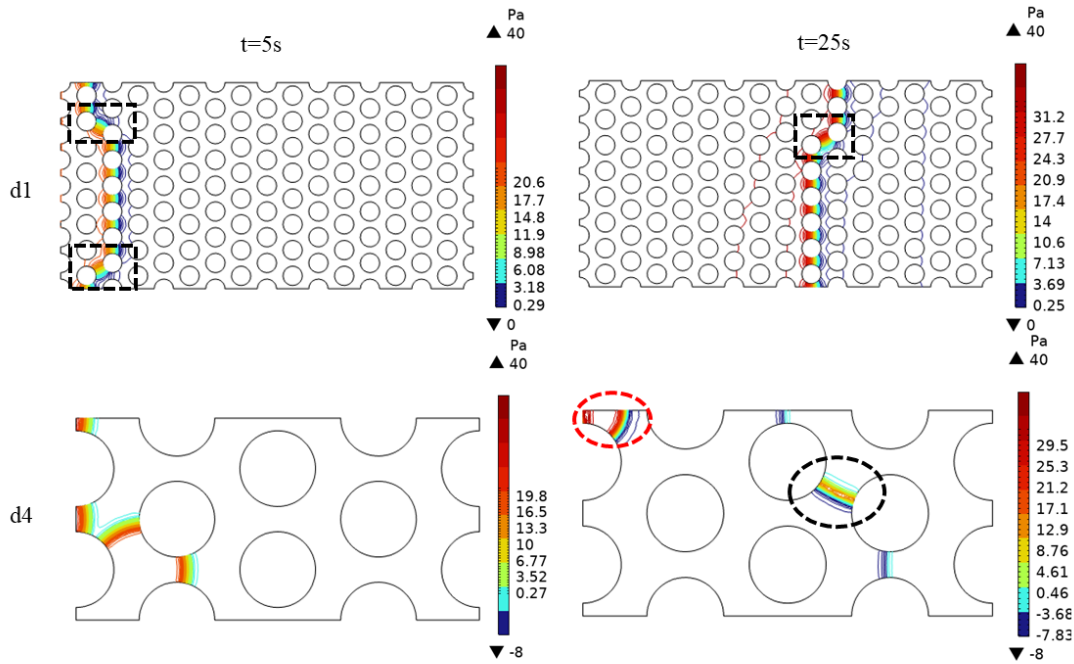
Fig. 8. Pressure contour distribution on d1 and d4.

the middle layer was completely saturated with water, initiating the next round of breakthroughs, and so forth. Termed the "queuing effect," this phenomenon was primarily caused by the uneven distribution of pressure differences.

Compared to d1, the water and air pressure contours of d4 were not symmetrically distributed, as shown in Fig. 8. At $t =$ 5 s, the water-air interface of d4 was blocked from reaching the lower pores. However, at this point, it was less affected by capillary resistance, and there existed a certain pressure difference on both sides of any water-air interface. As such, there was a small discrepancy in the seepage velocity of water in each direction, and the queuing effect was not pronounced. Moreover, due to the continuous compression of water on the residual air, for model d4, it was notably observed that the air pressure inside the bubble was higher than the water pressure outside the bubble at 25 s (Fig. 8, marked by the red circle of d4), resulting in increasing pressure inside the bubble. Additionally, at the water-air interface (Fig. 8, marked by black circles), it is evident that the pressure at the two-phase interface was larger, while the pressure on both sides of the water-air interface was lower. This phenomenon may be attributed to the turbulent flow rate at this location, which increased the pressure at the interface, surpassing the pressures of both water and air on either side of the interface.

3.2.2 Seepage field

The seepage field distributions of model d1 and d4 are illustrated in Fig. 9. An observation can be made that the water-air front of d1 reached the pores of the 3rd row at t = 5 s, while this area between the 2nd and 3rd rows remained unfilled by water, (refer to Fig. 5 for specific liquid surface positions). Due to the queuing effect, water in this region flowed from the

middle towards both top and bottom directions (Fig. 9, yellow arrow at 5 s in model d1). Nonetheless, the flow of water would displace the air between the 3rd and 4th rows from the top and bottom towards the middle, eventually generating convection that flowed backward (Fig. 9, red arrow at 5s in model d1). Instead, at 25 s, the water flowed from the top to the bottom, and the air in the next layer (between rows 12 and 13) flowed from the middle to up and down (Fig. 9, red arrow 25 s of Model d1). Therefore, in the infiltration process of fine pores, both water and air followed the queuing effect.

Model d4 only had two pores in the 2nd row due to its large grains. An observation can be made from Fig. 9 that the water-air front reached the lower pores at 5 s. At this moment, both the water and air arrows pointed towards the interface (Fig. 9, red circle of model d3), suggesting that water flow was blocked, leading water to preferentially infiltrate upward. Further, the darker hue of the upper pore indicated a greater velocity of water flow therewithin. Hence, the flow of water through the coarse pore was also subject to the queuing effect, although the effect was not obvious. At 25 s, the arrows at the water-air interface were more dispersed (Fig. 9, 25 s red circle of model d4). Compared with model d1, model d4 had a wider seepage channel, which was prone to turbulence at the water-air interface and eventually formed an unstable meniscus.

To summarize, according to the analysis of the pressure field and seepage field, an inference can be made that the queuing effect occurred in both coarse and fine pores during multi-row grain infiltration; however, there were notable distinctions. Water within the fine pores of d1 encountered significant capillary resistance, impeding water infiltration. Moreover, due to the abundance of rows, the water-air interface advanced uniformly. Conversely, in d4 with coarse pores and
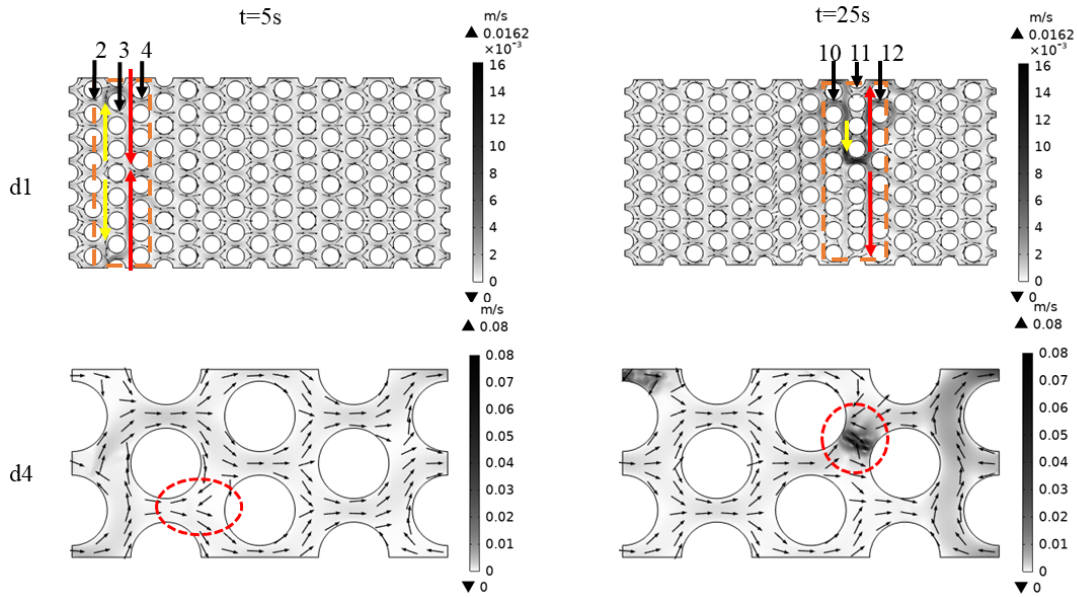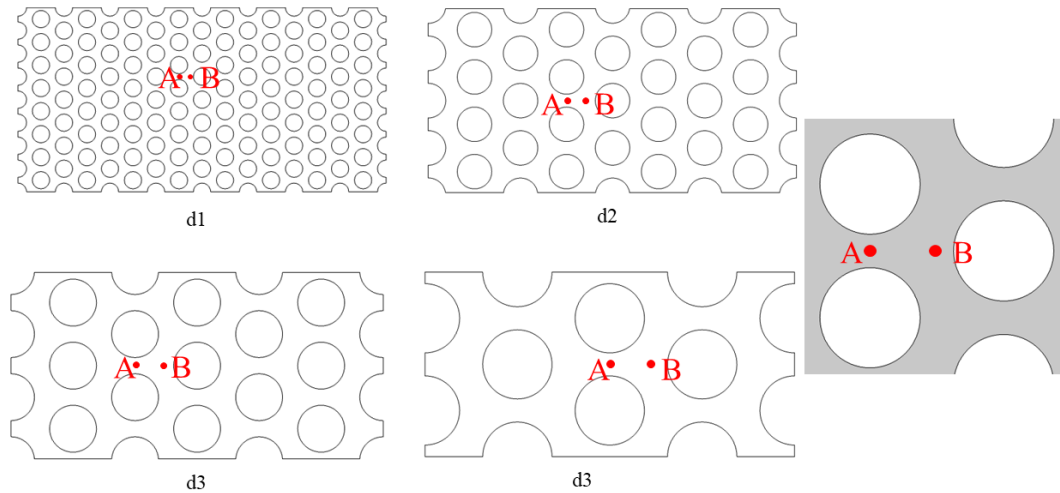
Fig. 9. Distribution of seepage arrows on d1 and d4.

Fig. 10. Location distribution of the two points A and B.

a smaller number of rows, uneven infiltration became more pronounced.

4. Discussion

4.1 Impact of pore size on pressure

As previously established, pore size exerts a significant impact on the pressure variation during the infiltration process; however, the analysis lacks precision. As discussed in this section, the influence of pore size on pressure change was illustrated by plotting the pressure curve at the intermediate point of the grain. Two points, A and B, situated between three adjacent grains were selected to plot the pressure variation diagram. Point A was positioned at the center of the vertical row of particles, and point B was on the same horizontal line as A. This is demonstrated in Fig. 10.

The pressure-time curves of points A and B in the four models are plotted in Fig. 11. An observation can be made that the evolution of both pressures with time in the four models exhibited a fluctuating pattern. Model d1 serves as an example to elucidate this feature. In the early stage of water infiltration, the pressure curve remained relatively flat. However, around 19 s, the pressure at point A began to rise rapidly following a slight fluctuation. Upon comparing the phase change diagram of d1, it is evident that the water-air interface reached point A at this time. Subsequently, as the water-air interface passed through point A, there was a sharp drop in pressure, followed by a significant increase upon reaching point B. After the first peak at point B, curves A and B coincided. After fluctuating up and down for a period until 40 s, the infiltration reached a stable pressure of 0 Pa. In addition, before the pressure of po-
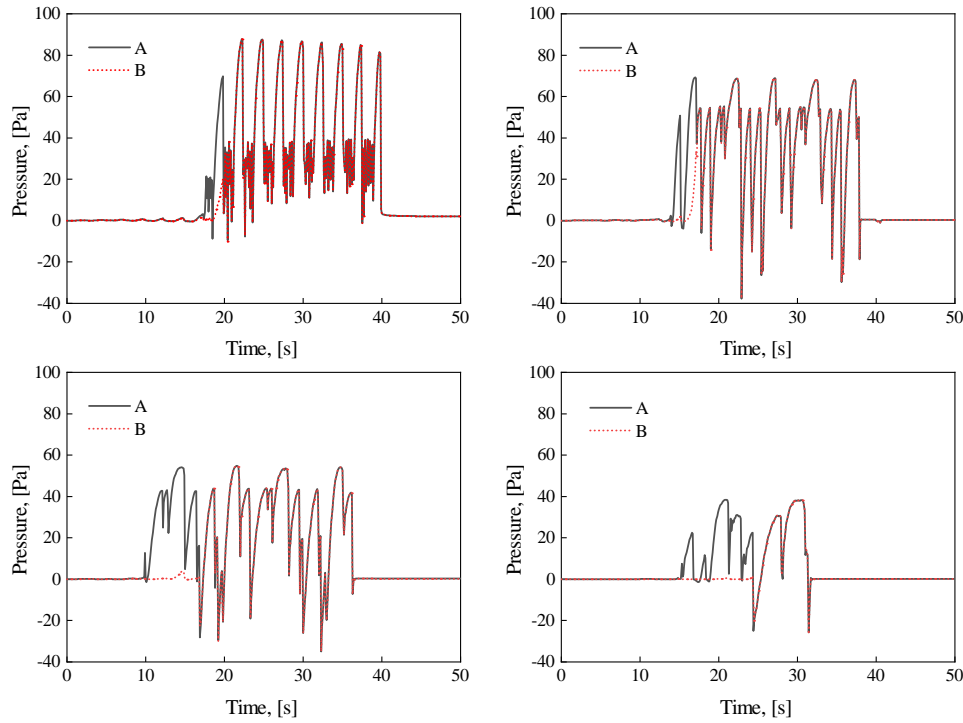
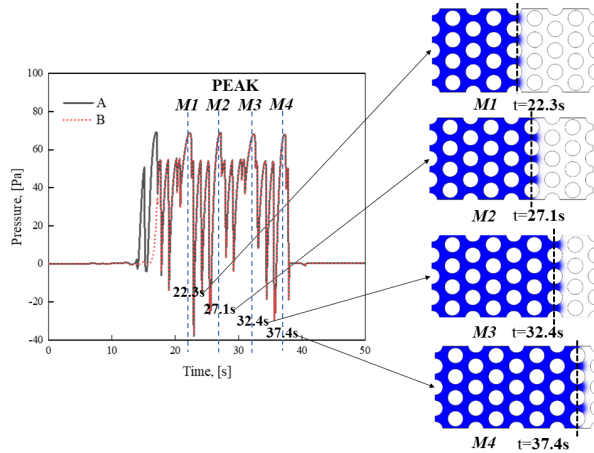**Fig. 11**. Pressure curves of two points A and B.

Fig. 12. The two-phase interface corresponding to the peak pressure in d2.

int A reached its peak, the four curves exhibited minor fluctuations. This occurred because when the water-air interface approached point A, it encountered capillary resistance and did not pass through immediately. Instead, it queued for infiltration until the middle layer was saturated with water. During the queuing infiltration process, fluid flow caused fluctuations in the water-air interface at point A. Consequently, these fluctuations resulted in small variations observed on the pressure curve before it reached its maximum value. In conclusion, the trend of pressure change was consistent in the four graphs, but the pressure values were quite different. In the infiltration process, the peak pressures of the two points A and B were 87.63, 68.68, 54.88 and 38.26 Pa, respectively.

During the seepage process, the pressure curves of B points in the four models fluctuated according to a waveform cycle until the seepage reached stability. At the same time, the fluctuation times of each waveform were related to the number of pore rows after point A. To investigate this relationship, model d2 was taken as an example, and the time corresponding to each wave peak was selected, as shown in Fig. 12. It is shown that the two-phase interface diagram corresponding to the time of the peak of the pressure curve at point b in Fig 11(b). As depicted, when $t = 22.3$s, the pressure at point B reached its first peak, coinciding with the water-air interface of the pore forming a straight line and being on the verge of breaking through. Following the breakthrough, the pressure value rapidly dropped, reaching the next peak again at $t = 27.1$s. With such cyclic fluctuations, the water-air interface corresponding to each peak pressure at point B occurred at the moment of imminent breakthrough. Due to the high resistance encountered by the water-air interface when penetrating the pores, the queuing effect initially occurred. Once the middle layer saturated, the water volume would progressively increase, leading to the eventual breakthrough. Throughout this process, the pressure would escalate quickly. After the breakthrough, water flow was influenced by inertial flow, leading to fast velocities as it passed through pores. As such, pressure dropped rapidly post-breakthrough until the middle layer was filled with water, initiating the next pressure cycle.

5. Conclusions

In the present study, under the condition of consistent porosity, four two-dimensional homogeneous numerical simulation models were created by varying the grain diameter to

control the pore width. The infiltration of water in different models was analyzed from various aspects. Based on the interpretation of the simulation results, the following conclusions can be drawn.

1) For the porous media model with the same porosity and similar pore structure, the pore size between grains had a significant effect on the infiltration law. In the porous media model with larger pores, the infiltration rate of water was faster, and the infiltration time to the stable moment was shorter. At the same injection speed, the infiltration time between models d1 and d4 differed by approximately 20%. However, the water saturation contradicted the aforementioned rule. Smaller pores resulted in higher water saturation and a more uniform infiltration. Conversely, larger pores tended to trap more residual air patches, resulting in lower saturation and reduced infiltration efficiency. The difference in final water saturation between model d1 and model d4 was approximately 18%. Although porous media with fine pores experienced greater capillary resistance due to narrow infiltration channels, making it difficult for fluid to pass through and resulting in a longer time for the fluid to reach stability, the overall advance of the water-air interface during seepage was relatively flat, and there was no large area of residual air.

2) The queuing effect was caused by the pressure difference. In the process of multi-row grain infiltration, there was a queuing effect regardless of pore size, but there were significant differences. Because of the smaller pores and higher number of rows, the queuing effect of model d1 was more obvious, and the water-air interface advanced uniformly. Conversely, in model d4 with coarse pores and a smaller number of rows, uneven infiltration became more pronounced.

3) For porous media with fine pore widths, the fluid needed to overcome greater capillary resistance when passing through the pores. When water passed through each row of pores, it would block the infiltration of water due to the influence of capillary resistance. Until the volume of water increased enough to complete the pore breakthrough. During water ingress, the pressure in the water-filled area would increase. Once the water-air interface was breached, the sudden flow rate surge would cause an instantaneous pressure drop. Under a constant inlet flow rate, the maximum overcoming pressures needed for the liquid to pass through four pores of varying sizes were 87.63, 68.68, 54.88, and 38.26 Pa, respectively.

Acknowledgements

Conflict of interest

The authors declare no competing interest.

References

Amiri, H. A., Hamouda, A. A. Evaluation of level set and phase field methods in modeling two phase flow with viscosity contrast through dual-permeability porous medium. International Journal of Multiphase Flow, 2023, 52: 22-34.

Bachu, S. Review of CO_2 storage efficiency in deep saline aquifers. International Journal of Greenhouse Gas Control, 2015, 40: 188-202.

Badalassi, V. E., Ceniceros, H. D., Banerjee, S. Computation of multiphase systems with phase field models. Journal of Computational Physics, 2023, 190(2): 371-397.

Beebe, D. J., Mensing, G. A., Walker, G. M. Physics and applications of microfluidics in biology. Annual review of biomedical engineering, 2002, 4(1): 261-286.

Bhagat, A. A. S., Bow, H., Hou, H. W., et al. Microfluidics for cell separation. Medical & Biological Engineering & Computing, 2010, 48: 999-1014.

Cai, J., Chen, Y., Liu, Y., et al. Capillary imbibition and flow of wetting liquid in irregular capillaries: A 100-year review. Advances in Colloid and Interface Science, 2022, 304: 102654.

Cai, J., Jin, T., Kou, J., et al. Lucas-Washburn equation-based modeling of capillary-driven flow in porous systems. Langmuir, 2021, 37: 1623-1636.

Cai, J., Perfect, E., Cheng, C. L., et al. Generalized modeling of spontaneous imbibition based on Hagen-Poiseuille flow in tortuous capillaries with variably shaped apertures. Langmuir, 2014, 30(18): 5142-5151.

Cao, S. C., Dai, S., Jung, J. Supercritical CO_2 and brine displacement in geological carbon sequestration: Micro-model and pore network simulation studies. International Journal of Greenhouse Gas Control, 2016, 44: 104-114.

Celia, M. A., Reeves, P. C., Ferrand, L. A. Recent advances in pore scale models for multiphase flow in porous media. Reviews of Geophysics, 1995, 33: 1049-1057.

Golparvar, A., Zhou, Y., Wu, K., et al. A comprehensive review of pore scale modeling methodologies for multiphase flow in porous media. Advances in Geo-Energy Research, 2018, 2(4): 418-440.

Cottin, C., Bodiguel, H., Colin, A. Drainage in two-dimensional porous media: From capillary fingering to viscous flow. Physical Review E, 2010, 82(4): 046315.

Culligan, P. J., Barry, D. A., Parlange, J. Y., et al. Infiltration with controlled air escape. Water Resources Research, 2000, 36(3): 781-785.

Gravesen, P., Branebjerg, J., Jensen, O. S. Microfluidics-a review. Journal of micromechanics and microengineering, 1993, 3(4): 168.

Hirt, C. W., Nichols, B. D. Volume of fluid (VOF) method

for the dynamics of free boundaries. Journal of Computational Physics, 1981, 39(1): 201-225.

Hizir, F. E., Hardt, D. E. Effect of Substrate contact angle on ink transfer in flexographic printing. Paper Presented at Comsol Conference, Boston, USA, 7-9 October, 2014.

Hu, R., Lan, T., Wei, G. J., et al. Phase diagram of quasi-static immiscible displacement in disordered porous media. Journal of Fluid Mechanics, 2019, 875: 448-475.

Hu, R., Wan, J., Kim, Y., et al. Wettability impact on supercritical CO_2 capillary trapping: Pore-scale visualization and quantification. Water Resources Research, 2017, 53(8): 6377-6394.

Li, G., Zhan, L., Chen, Y., et al. Effects of flow rate and pore size variability on capillary barrier effects: A microfluidic investigation. Canadian Geotechnical Journal, 2022, 60(6): 902-916.

Li, G., Zhan, L., Zhang, Z., et al. Pore network modeling of capillary barrier effects: Impact of pore sizes. Canadian Geotechnical Journal, 2023, 61(1): 174-182.

Li, Q., Luo, K. H., Kang, Q. J., et al. Lattice Boltzmann methods for multiphase flow and phase-change heat transfer. Progress in Energy and Combustion Science, 2016, 52: 62-105.

Mirjalili, S., Jain, S. S., Dodd, M. Interface-capturing methods for two-phase flows: An overview and recent developments. Center for Turbulence Research Annual Research Briefs, 2017, pp: 117-135.

Morrow, N. R., Mason, G. Recovery of oil by spontaneous imbibition. Current Opinion in Colloid & Interface Science, 2001, 6(4): 321-337.

Osher, S., Fedkiw, R. P. Level set methods: An overview and some recent results. Journal of Computational Physics, 2001, 169(2): 463-502.

Patiño, I. D., Nieto-Londoño, C. Boundary element techniques for multiscale filling simulations in dual-scale fibrous reinforcements using two lumped approaches. Computational Mechanics, 2021, 68(6): 1223-1266.

Rokhforouz, M. R., Akhlaghi Amiri, H. A. Phase-field simulation of counter-current spontaneous imbibition in a fractured heterogeneous porous medium. Physics of Fluids,

2017, 29(6): 062104.

Stone, H. A., Kim, S. Microfluidics: Basic issues, applications, and challenges. AIChE Journal, 2001, 47(6): 1250.

Takada, N., Tomiyama, A. A numerical method for two-phase flow based on a phase-field model. JSME International Journal Series B Fluids and Thermal Engineering, 2006, 49(3): 636-644.

Vincent-Dospital, T., Moura, M., Toussaint, R., et al. Stable and unstable capillary fingering in porous media with a gradient in grain size. Communications Physics, 2022, 5(1): 306.

Wang, J., Fuentes, C. A., Zhang, D., et al., Wettability of carbon fibres at micro-and mesoscales. Carbon, 2017, 120: 438-446.

Wang, S., Feng, Q., Dong, Y., et al. A dynamic pore-scale network model for two-phase imbibition. Journal of Natural Gas Science and Engineering, 2015, 26: 118-129.

Wei, H., Sha, X., Chen, L., et al. Visualization of multiphase reactive flow and mass transfer in functionalized microfluidic porous media. Small, 2024, 20(32): 2401393.

Yan, G., Li, Z., Galindo Torres, S. A., et al. Transient two-phase flow in porous media: a literature review and engineering application in geotechnics. Geotechnics, 2022, 2(1): 32-90.

Zhang, Q., Yang, Y., Wang, D., et al. Correlations of residual oil distribution with pore structure during the water flooding process in sandstone reservoirs. Advances in Geo-Energy Research, 2024, 12(2): 113-126.

Zhan, L. T., Li, G. Y., Bate, B., et al. A preliminary exploration of the micro-scale behaviour of capillary barrier effect using microfluidics. Géotechnique, 2021, 73(6): 553-560.

Zhao, B., MacMinn, C. W., Primkulov, B. K., et al. Comprehensive comparison of pore-scale models for multiphase flow in porous media. Proceedings of the National Academy of Sciences of the United States of America, 2019, 116(28): 13799-13806.

Zhu, G., Yao, J., Zhang, L., et al. Investigation of the dynamic contact angle using a direct numerical simulation method. Langmuir, 2016, 32(45): 11736-11744.